A reversal in global terrestrial stilling and its implications for wind energy production

Zhenzhong Zeng[1,2]*, Alan D. Ziegler[3], Timothy Searchinger[4], Long Yang[5], Anping Chen[6], Kunlu Ju[7], Shilong Piao[8], Laurent Z. X. Li[9], Philippe Ciais[10], Deliang Chen[11], Junguo Liu[1], Cesar Azorin-Molina[11,12], Adrian Chappell[13], David Medvigy[14], Eric F. Wood[2]

[1] School of Environmental Science and Engineering, Southern University of Science and Technology, Shenzhen 518055, China

[2] Department of Civil and Environmental Engineering, Princeton University, Princeton, New Jersey 08544, USA

[3] Geography Department, National University of Singapore, 1 Arts Link Kent Ridge, Singapore 117570, Singapore

[4] Woodrow Wilson School, Princeton University, Princeton, New Jersey 08544, USA

[5] School of geography and ocean science, Nanjing University, Nanjing, Jiangsu Province, China

[6] Department of Biology, Colorado State University, CO 80523, USA

[7] School of Economics and Management, Tsinghua University, Beijing 100084, China

[8] Sino-French Institute for Earth System Science, College of Urban and Environmental Sciences, Peking University, Beijing 100871, China

[9] Laboratoire de Météorologie Dynamique, CNRS, Sorbonne Université, Ecole Normale Supérieure, Ecole Polytechnique, 75252 Paris, France

[10] Laboratoire des Sciences du Climat et de l'Environnement, UMR 1572 CEA-CNRS-UVSQ, 91191 Gif-sur-Yvette, France

[11] Regional Climate Group, Department of Earth Sciences, University of Gothenburg, Gothenburg, Sweden

[12] Centro de Investigaciones sobre Desertificación, Consejo Superior de Investigaciones Cientificas (CIDE-CSIC), Montcada, Valencia, Spain

[13] School of Earth and Ocean Sciences, Cardiff University, Wales, CF10 3AT, UK

[14] Department of Biological Sciences, University of Notre Dame, Notre Dame, IN 46556, USA

*Correspondence to: zzeng@princeton.edu

Manuscript for *Nature Climate Change*

September 29, 2019

Wind power, a rapidly growing alternative energy source, has been threatened by reductions in global average surface wind speed that have been occurring over land since the 1980s, a phenomenon known as global terrestrial stilling. Here, we use wind data from *in-situ* stations worldwide to show that the stilling reversed around 2010 and global wind speeds over land have recovered. We illustrate that decadal-scale variations of near-surface wind are likely dertermined by internal decadal ocean/atmosphere oscillations, rather than vegetation growth and/or urbanization as hypothesized previously. The strengthening has increased potential wind energy by 17 ±2% for 2010-2017, boosting U.S. wind power capacity factor by ~2.5% that explains half the increase in U.S. wind capacity since 2010. In the longer-term, the use of ocean/atmosphere oscillations to anticipate future wind speeds could allow optimization of turbines for expected speeds during their productive life spans.

Reports of a global decline in land surface wind speed of 8% from ~1980 to 2010 have raised concerns about outputs from future wind power[1-5]. Wind power (p) varies with the cube of wind speed (u) according to the formula

$$p = \frac{\rho s f}{2} u^3 \quad (1),$$

where ρ is air density, s the swept area of the turbine, and f an efficiency factor[6]. The decline has been manifest in the northern mid-latitude countries where the majority of wind turbines are installed including China, the U.S. and Europe[1]. If the observed trend from 1980 to 2010 were to continue to the end of the century, global u would reduce by 21%, halving the amount of power available in the wind (using Equation (1)). Understanding the drivers of this long-term decline in wind speed is critical not merely to maximize wind energy production[7-9] but also to address other globally significant environmental problems related to stilling, including reduced aerosol dispersal, changes in evapotranspiration rates, and adverse effects on animal behavior and ecosystem functioning[1,3,4,10].

The potential causes for the global terrestrial stilling are complex and remain contested[2,3,11,12]. Many regional-scale studies[13-17] using reanalysis datasets have found correlations of u with various climate indices. Those studies hypothesize that terrestrial stilling is caused by changes in large-scale circulations[11], which appear as consistent wind speed changes at the surface and at higher levels in reanalysis datasets[11,14]. Nevertheless, there are large uncertainties in these datasets[2,11,14], and more importantly, global terrestrial stilling is either not reproduced or has been largely underestimated in global reanalysis products[2,11] (Supplementary Fig. 1) and/or climate model simulations for IPCC AR5 (Supplementary Fig. 2). Acknowledging that wind speed reanalysis datasets do not represent land surface dynamics, the discrepancies between the decreasing trends derived from *in-situ* stations and from reanalysis or climate model simulations lead to the hypothesis that global terrestrial stilling is caused by increased drag related to increased surface roughness from the greening of the Earth and/or urbanization[2,18], both of which would suggest further declines in the future.

However, conversely, recent studies have described wind speed reversal at local scales[19,20] or an increase of global wind speed during a particular year[21], despite uncertainty over the global trend of wind speed change[5,11]. The recent reversal over land, if evidenced to be true at the global scale, could elucidate the causes of global terrestrial stilling and potentially improve future wind energy projections.

Analysis

We integrate direct *in-situ* observations of u from ground weather stations from 1978 to 2017 together with statistical models for detection of trends. The stations, mainly distributed in the northern mid-latitudes countries, were carefully selected from the Global Summary of Day (GSOD) database following strict quality control procedures (Supplementary Fig. 3; see *Methods* for details). To test for a continuation of the terrestrial stilling after 2010 (refs 1-3), we use a piecewise linear regression model to examine the potential trend changes[22,23].

Scope of a reversal in global terrestrial stilling

The analysis shows that global mean annual u decreased significantly at a rate of -0.08 m s^{-1} (or -2.3%) per decade during the first three decades beginning in 1978 (P-value < 0.001; Fig. 1a, Supplementary Table 1). While the decreasing trend has previously been shown[2-4] and confirms global terrestrial stilling as an established phenomenon during the period of 1978-2010, we find that u has significantly increased in the current decade. This turning point is statistically significant at $P < 0.001$ with a goodness of fit of an $R^2 = 90\%$ (Fig. 1a). The recent increasing rate of 0.24 m s^{-1} decade^{-1} ($P < 0.001$) is three-fold the decreasing rate before the turning point in 2010.

To exclude the possibility that the turning point is caused by large wind speed changes at only a few sites, we repeat our analyses 300 times by randomly resampling 40% of the global stations each time (grey lines in Fig. 1a; 40% of the stations are selected to ensure a sufficient sample size ($n > 500$)). We find significant turning points in each randomly-selected sub-sample ($P < 0.001$; $R^2 \geq 76\%$). Run-specific turning points occur between 2002 and 2011, with most (95%) of them between 2009 and 2011 (Fig. 1b). In addition, mean annual *u* changes before and after a specific turning point based on the 300 sub-sample estimates are -0.08 ± 0.01 m s^{-1} per decade and 0.24 ± 0.03 m s^{-1} per decade, respectively (Fig. 1c), identical to those values based on all global samples.

Spatial analyses further confirm that the recent reversal is a global-scale phenomenon (Supplementary Fig. 4a-c). A majority (79%) of the stations where *u* decreased significantly during 1978-2010 (Supplementary Fig. 4b) have positive trends after 2010 (Supplementary Fig. 4c). The stations are mainly distributed over North America, Europe, and Asia. Significant turning points exist in all the three regional mean annual *u* time series ($P < 0.001$, Supplementary Fig. 4d-f), but they vary in the specific year of occurrence. For example, a turning point occurs earlier in Asia (2001, R^2 =80%, Supplementary Fig. 4f) and Europe (2003, R^2 = 56%, Supplementary Fig. 4e) than in North America (2012, R^2 = 80%, Supplementary Fig. 4d). Nevertheless, all the three regions have the most significant increase in *u* after ~2010 (Supplementary Fig. 4d-f).

The existence of turning points is robust regardless of season (Supplementary Table 1 and Supplementary Fig. 5) or wind variable chosen for analysis (Supplementary Fig. 6), and shows no dependence on quality control procedures for weather station data (Supplementary Fig. 7). For maximum sustained wind and wind gusts, the turning points appear earlier and the recent increasing rates are weaker (Supplementary Fig. 6). Furthermore, we show that our findings are robust and repeatable (Supplementary Fig. 8) using a different data set—the HadISD database, which follows station selection criteria and a suite of quality control tests established by Met

Office Hadley Centre[24]. We also find that the tendency for an increasing number of stations becoming automated during recent decades (Supplementary Figs 9 and 10) does not affect the result (Supplementary Fig. 11). Finally, to test the effect of inhomogeneity, we remove all the stations with change points detected by Pettitt tests[25]. After removal, the results do not change when the analysis is repeated (Supplementary Fig. 12). All these lines of evidence provide independent support that the trends in u are not caused by changes in measurement methods and inhomogeneity.

Causes of the reversal in global terrestrial stilling

A variety of theories have been presented previously to explain stilling, many of which focus on the drag force of u linked to increased terrestrial roughness caused by urbanization and/or vegetation changes[2,12]. These theories are debated[26] (also see Supplementary Figs 13 and 14). Our finding of a global stilling change after 2010, and especially the finding of an increasing rate which is three times that of the decreasing rate before 2010 (Fig. 1a), are counter to these theories because terrestrial roughness did not suddenly change in 2010. More likely, the variation in u (including prior stilling and the recent reversal) is determined mainly by driving forces associated with decadal variability of large-scale ocean/atmospheric circulations.

Wind is created by pressure gradients associated with uneven heating of the Earth surface (temperature anomalies or heterogeneity), and the latter is to a large extent described by climate indices for oscillations. To test such associations, we first include twenty-one climate indices in the pool of indicators for ocean/atmosphere oscillations (Supplementary Table 2 and *Methods*). To avoid overfitting, we apply stepwise regression[27] to identify six largest explanatory power factors for the decadal variations of *u* over the globe, North America, Europe, and Asia, respectively (see Supplementary Table 3). The reconstructed *u* obtained from the stepwise linear regression matches well with the observed *u* (Supplementary Figs 15 and 16, and discussion in *Methods*). Finally, we train our models using only the detrended time series before the turning points (2010 for the globe, 2012 for North America, 2003 for Europe, and 2001 for Asia), finding that the models are capable of reproducing the positive trends after the turning points, not only for the globe ($P < 0.001$; Fig. 2a), but also for all the three regions ($P < 0.001$; Fig. 2b-d). The magnitude of the increasing rate after the turning points is well modelled (Fig. 2). These results suggest a predictive relationship between wind changes and ocean/atmosphere oscillations, which would be very valuable for the wind energy sector.

We further construct the composite annual mean surface temperature for the years that exhibit negative (Fig. 3a) and positive (Fig. 3b) anomalies of detrended *u*. During the years of negative *u* anomalies (Fig. 3a) the following are observed: (a) positive anomalies of temperature prevail over the tropical northern Atlantic (5.5^{o}N to 23.5^{o}N, 15^{o}W to 57.5^{o}W), showing a positive value for Tropical Northern Atlantic Index (TNA); (b) the west (east) Pacific is warmer (colder) than normal years, demonstrating a negative value for Pacific Decadal Oscillation (PDO); and (c) positive anomalies of temperature occur near the Azores and negative anomalies occur over Greenland, indicating a negative value for North Atlantic Oscillation (NAO). The opposite pattern (i.e. negative TNA, positive PDO and NAO) occurs during the years of positive *u* anomalies (Fig. 3b). Furthermore, TNA has strong, significant, and negative correlations with regional *u*, in particular, over North America (Fig. 3c); PDO has significant positive correlations with regional *u* globally (Fig. 3e); and NAO has overwhelmingly significant positive correlations with regional u in the U.S. and Northern Europe, but negative correlations with regional u in Southern Europe (Fig. 3d). These patterns are consistent with the finding that the greatest explanatory power factor is TNA for North America ($R = -0.67$, $P < 0.001$), PDO for Asia ($R = 0.50$, $P < 0.01$), and NAO for Europe ($R = 0.37$, $P < 0.05$) (for more discussion refer to *Methods*). The ocean/atmosphere oscillations, characterized as the decadal variations in these climate indices (mainly TNA, NAO, PDO), can therefore explain the decadal variation of u (i.e., the long-term stilling and the recent reversal) (Figs 2 and 3f-h).

Several theories[28-31] have tried to provide potential physical mechanisms describing how different ocean/atmosphere oscillations affect regional u over land. With respect to TNA, prior studies demonstrate that the positive phase of TNA is linked with a weakened Hadley circulation (details of the theory refer to ref. 28). We also find that during the positive phase of TNA there is a cold anomaly over the eastern coast of the U.S. (Fig. 3a and ref. 28). This pattern leads to a southward component of surface wind and a stable environment of weak convergence from the tropics to the mid-latitudes, resulting a reduction of u in the mid-latitudes, the U.S. in particular (Fig. 3c and Supplementary Fig. 17a,b). As for NAO, its negative and positive phases have different jet stream configurations and wind systems in Northern versus Southern Europe (Supplementary Fig. 17c,d; refer to ref. 29). During the positive (negative) phase, the pressure gradient across the North Atlantic[29] generates strong winds and storms across Northern (Southern) Europe (Supplementary Fig. 17c,d), explaining the contrasting correlations of NAO to u in these two regions (Fig. 3d, Supplementary Fig. 18). For PDO, the temperature gradient during the negative (positive) phase generates an easterly (westerly) component of surface wind (refer to refs 30, 31), which weakens (strengthens) the prevailing westerly winds in the mid-latitudes (Supplementary Fig. 17e,f) and explains the widespread and significant positive correlations between PDO and *u* across the whole mid-latitudes (Fig. 3e). However, despite these potential physical mechanisms[28-31], the relationships between ocean/atmosphere oscillations and long-term wind speeds over land are still uncertain and require more investigations.

Finally, it is critical to determine why global reanalysis products do not reproduce or underestimate the historical terrestrial stilling (Supplementary Fig. 1), which is a major basis for prior studies[2,12] rejecting ocean/atmosphere oscillations as a dominant driver for terrestrial stilling. While global reanalysis products are generated at numerical weather prediction centers with advanced data assimilation systems, most cannot assimilate near-surface winds over land properly due to inappropriate model topography and inaccuarency of atmospheric boundary layer processes that are implemented into the data assimilation systems. ERA-Interim[32], one of the best products available, can only assimilate surface winds over seas from scatterometers, ships and bouys. The capacities of these products in reproducing the near-surface wind speed over land are thus generally poor and rely on climate models. We find that in the regions where AMIP model simulations (i.e. atmospheric simulations forced with observed sea surface temperature) capture the stilling, such as Europe and India (Fig. 4a,b in ref. 26), the global reanalysis products are also capable of reproducing the stilling (Fig. S1c). In constrast, for regions where AMIP simulations do not capture the stilling, such as North America[26,33], the global reanalysis products also fail to reproduce the stilling[2,11] (Fig. S1b). Model limitations therefore are likely the reason preventing global reanalysis products from reproducing the observed near-surface wind speed changes in some regions. More efforts are required to improve surface process parameterization scheme and its connection to ocean/atmosphere circulations in climate models and operational weather data assimilation systems.

Implications for wind energy production

In wind power assessments, near-surface wind observations from weather stations (u at the height of z_r = 10 meters) are often used to estimate wind speeds at the height of a turbine (u_{tb} at the height of z_{tb} = 50-150 meters) using an exponential wind profile power law relationship:

$$u_{tb} = u\left(\frac{z_{tb}}{z_r}\right)^{\alpha} \tag{2}$$

where the α is commonly assumed to be constant (1/7) in wind resource assessments because the differences between these two levels are unlikely great enough to introduce considerable errors in the estimates[5].

Changes in wind speed matter not only on average but also in the percentage of time wind speeds are high or low. A velocity of u_{tb} > 3 m s^{-1} is a typical minimum value needed to drive turbines efficiently and therefore, wind speeds below 3 m s^{-1} are typically wasted from the power generation perspective. Although periods of high wind speed greatly increase the physical capacity to generate power according to formula (1), turbines are built with a maximum capacity, so periods of high wind speed can also “waste” the uses of wind with the threshold depending on the capacity of the turbine.

On average, the increase of global mean annual u from 3.13 m s^{-1} in 2010 to 3.30 m s^{-1} in 2017 (Fig. 1a; see *Methods* for details) increases the amount of energy entering a hypothetical wind turbine receiving the global average wind by 17 ±2% (uncertainty is associated with subsamples in Fig. 1a; regionally, 22 ±2% for North America, 22 ±4% for Europe, and 11 ±4% for Asia). At the hourly scale, the frequency of low u decreases while the frequency of high u increases (Fig. 4a). Using one General Electric GE 2.5 – 120 turbine[34] (Supplementary Fig. 19) for illustration, the effects of changes in global average u increase potential power generation from 2.4 million kWh in 2010 to 2.8 million kWh in 2017 (+17%). If the present trend persists for at least another decade, in light of the robust increasing rate during 2000-2017 (Fig. 1a) and the long cycles of natural ocean/atmosphere oscillations[28-31,35] (Supplementary Fig. 20), power would rise to 3.3 million kWh in 2024 (+37%), resulting in a +3% per decade increase of global-average capacity factor (mean power generated divided by rated peak power). This change is even larger than the projected change in wind power potential caused by climate change under multi-scenairos[36].

During the past decade, the capacity factor of the U.S. wind fleet[37] has steadily risen at a rate of +7% per decade (Fig. 4b), previously attributed solely to technology innovations[38]. We find that the capacity factor for wind generation in the U.S. is highly and significantly correlated with the variation in the cube of regional-average u (u^3, $R = 0.86$, $P < 0.01$; Fig. 4b). To isolate the u-induced increase in capacity factor from that due to technology innovations, we use the regional mean hourly wind speed in 2010 and 2017 to estimate the increase of capacity factor for a given turbine, thereby controlling for technology innovations. It turns out that the increased u^3 explains ~50% of the increase of the capacity factor (see *Methods* for details). Therefore, in addition to technology innovations, the strengthening u is another key factor powering the increasing reliability of wind power in the U.S. (and other mid-latitude countries where u is increasing, such as China and European countries).

To illustrate the consequences, one turbine (General Electric GE 1.85 – 87 (ref. 39)) installed at one of our *in-situ* weather stations in the U.S. in 2014 (inset plot in Fig. 4c), which was expected to produce 1.8 ±0.1 million kWh using four years of *u* records before the installation (2009-2013)[39], actually produced 2.2 ±0.1 million kWh between 2014-2017 (+25%). This system has the potential to generate 2.8 ±0.1 million kWh (+56%) if *u* recovers to the 1980s level (red bars in Fig. 4d; see *Methods* for details). Globally, 90% of the global cumulative wind capacity has been installed in the last decade[40], during which global *u* has been increasing (see above).

Discussion

Although the response of ocean/atmosphere oscillations to anthropogenic warming remains unclear[31], the increases in wind speeds should continue for at least a decade because these oscillations change over decadal time frames[28-31,35]. Climate model simulations constrained with historical sea surface temperature also show a long cycle in *u* over land (Supplementary Fig. 20). Our findings are therefore good news for the power industry for the near future.

However, oscillation patterns in the future will likely cause returns to declining wind speeds, and anticipating these changes should be important for the wind power industry. Wind farms should be constructed in the areas with stable winds and high effective utilization hours (e.g. 3 - 25 m s^{-1}). If high wind speeds are likely to be common, building turbines with larger capacities could be justified. For example, capturing more available wind energy (blue bars in Fig. 4d) could be achieved through the installation of higher capacity wind turbines (e.g. General Electric GE 2.5 – 120, green bars in Fig. 4d), greatly increasing total power generation. Most turbines tend to require replacement after 12-15 years[41]. Further refinement of the relationships uncovered in this paper could allow choices of turbine capacity, rotor and tower that are optimized not just to wind speeds of the recent past but to likely future changes during the lifespan of the turbines.

In summary, we find that after several decades of global terrestrial stilling, wind speed has rebounded, increasing rapidly in the recent decade globally since 2010. Ocean/atmosphere oscillations, rather than increased surface roughness, are likely the causes. These findings are important for those vested in maximizing the potential of wind as an alternative energy source. The development of renewable energy sources including wind power[6-9,40] is central to energy scenarios[8] that help keep warming well below 2 ◦C. One megawatt (MW) of wind power reduces 1,309 tonnes of CO_2 emissions and also saves 2,000 liters of water compared with other energy sources[9,40]. Since its debut in the 1980s, the total global wind power capacity reached 539 gigawatts by the end of 2017, and the wind power industry is still booming globally. For instance, the total wind power capacity in the U.S. alone is projected to increase fourfold by 2050 (ref. 9). The reversal in global terrestrial stilling bodes well for the expansion of large-scale and efficient wind power generation systems in these mid-latitude countries in the near future.

References.

1. Roderick, M. L., Rotstayn, L. D., Farquhar, G. D. & Hobbins, M. T. On the attribution of changing pan evaporation. *Geophys. Res. Lett.* **34,** 1–6 (2007).

2. Vautard, R., Cattiaux, J., Yiou, P., Thépaut, J. N. & Ciais, P. Northern Hemisphere atmospheric stilling partly attributed to an increase in surface roughness. *Nat. Geosci.* **3,** 756–761 (2010).

3. Mcvicar, T. R., Roderick, M. L., Donohue, R. J. & Van Niel, T. G. Less bluster ahead? ecohydrological implications of global trends of terrestrial near-surface wind speeds. *Ecohydrology* **5,** 381–388 (2012).

4. McVicar, T. R. *et al.* Global review and synthesis of trends in observed terrestrial near-surface wind speeds: Implications for evaporation. *J. Hydrol.* **416–417,** 182–205 (2012).

5. Tian, Q., Huang, G., Hu, K. & Niyogi, D. Observed and global climate model based changes in wind power potential over the Northern Hemisphere during 1979–2016. *Energy* **167,** 1224–1235 (2019).

6. Lu, X., McElroy, M. B. & Kiviluoma, J. Global potential for wind-generated electricity. *Proc. Natl. Acad. Sci.* **106,** 10933–10938 (2009).

7. UNFCCC. *Adoption of the Paris Agreement* (FCCC/CP/2015/L.9/Rev.1., 2015).

8. IPCC. *Summary for policymakers in Climate change 2014: Mitigation of climate change. Contribution of working group III to the fifth assessment report of the Intergovernmental Panel on Climate Change* (O. Edenhofer et al., Eds., Cambridge University Press, Cambridge, UK and New York, USA, 2014).

9. U.S. Department of Energy. *Projected growth wind industry now until 2050* (Washington, D.C., 2018).

10. Nathan, R. & Muller-landau, H. C. Spatial patterns of seed dispersal, their determinants and consequences for recruitment. *Trends Ecol. Evol.* **15,** 278–285 (2000).

11. Torralba, V., Doblas-Reyes, F. J. & Gonzalez-Reviriego, N. Uncertainty in recent near-surface wind speed trends: a global reanalysis intercomparison. *Environ. Res. Lett.* **12,** 114019 (2017).

12. Wu, J., Zha, J. L., Zhao, D. M. & Yang, Q. D. Changes in terrestrial near-surface wind speed and their possible causes: an overview. *Clim. Dyn.* **51,** 2039–2078 (2018).

13. Nchaba, T., Mpholo, M. & Lennard, C. Long-term austral summer wind speed trends over southern Africa. *Int. J. Climatol.* **37,** 2850–2862 (2017).

14. Chen, L., Li, D. & Pryor, S. C. Wind speed trends over China: quantifying the magnitude and assessing causality. *Int. J. Climatol.* **33,** 2579–2590 (2013).

15. Naizghi, M. S. & Ouarda, T. B. Teleconnections and analysis of long-term wind speed variability in the UAE. *Int. J. Climatol.* **37,** 230–248 (2017).

16. Guo, H., Xu, M. & Hu, Q. Changes in near-surface wind speed in China: 1969-2005. *Int. J. Climatol.* **31**, 349-358 (2011).

17. Wu, J., Zha, J. L., Zhao, D. M. & Yang, Q. D. Changes of wind speed at different heights over Eastern China during 1980-2011. *Int. J. Climatol.* **38**, 4476-4495 (2018).

18. Zhu, Z. *et al.* Greening of the Earth and its drivers. *Nat. Clim. Chang.* **6,** 791–796 (2016).

19. Kim, J. C. & Paik, K. Recent recovery of surface wind speed after decadal decrease: a focus on South Korea. *Clim. Dyn.* **45,** 1699–1712 (2015).

20. Azorin-Molina, C. *et al.* Homogenization and assessment of observed near-surface wind speed trends over Spain and Portugal, 1961-2011. *J. Clim.* **27,** 3692–3712 (2014).

21. Tobin, I., Berrisford, P., Dunn, R. J. H., Vautard, R. & McVicar, T. R. [Global climate; Atmospheric circulation] Surface winds [in "State of the Climate in 2013". *Bull. Am. Meteorol. Soc.* **95,** S28-S29 (2014).

22. Toms, J. D. & Lesperance, M. L. Piecewise regression: a tool for identifying ecological thresholds. *Ecology* **84,** 2034–2041 (2003).

23. Ryan, S. E. & Porth, L. S. *A tutorial on the piecewise regression approach applied to bedload transport data* (2007).

24. Dunn, R. J. H., Willett, K. M., Morice, C. P. & Parker, D. E. Pairwise homogeneity assessment of HadISD. *Clim. Past* **10,** 1501–1522 (2014).

25. Pettitt A. N. A non-parametric approach to the change-point problem. *J. R. Stat. Soc. Ser. C: Appl. Stat.* **28,** 126–135 (1979).

26. Zeng, Z. *et al.* Global terrestrial stilling: does Earth's greening play a role? *Environ. Res. Lett.* **13,** 124013 (2018).

27. Draper, N. R. & Smith, H. *Applied Regression Analysis, 3rd Edition* (Wiley-Interscience, 1998).

28. Wang, C. Z. Atlantic climate variability and its associated atmospheric circulation cells. *J. Clim.* **15,** 1516–1536 (2002).

29. Hurrell, J. W., Kushnir, Y., Ottersen, G. & Visbeck, M. *The North Atlantic Oscillation climatic significance and environmental impact* (eds. Hurrell, J. W., Kushnir, Y., Ottersen, G. & Visbeck, M., 2003).

30. Zhang, Y., Xie, S.-P., Kosaka, Y. & Yang, J.-C. Pacific decadal oscillation: Tropical Pacific forcing versus internal variability. *J. Clim.* **31,** 8265–8279 (2018).

31. Timmermann, A. *et al.* El Niño-Southern Oscillation complexity. *Nature* **559,** 535–545

(2018).
32. Dee, D. P. *et al.* The ERA-Interim reanalysis: configuration and performance of the data assimilation system. *Q J. Roy. Meteor Soc.* **137,** 553–597 (2011).
33. Pryor, S. C. *et al*. Wind speed trends over the contiguous USA. *J. Geophys. Res. D: Atmos.* **114,** D14105 (2009).
34. Wind-turbine-models.com. General Electric GE 2.5 - 120. (2018). at https://www.en.wind-turbine-models.com/turbines/310-general-electric-ge-2.5-120
35. Steinman, B. A. *et al.* Atlantic and Pacific multidecadal oscillations and Northern Hemisphere temperatures. *Science* **347,** 988-991(2015).
36. Tobin, I. *et al.* Climate change impacts on the power generation potential of European mid-century wind farms scenario. *Environ. Res. Lett.* **11,** 034013 (2016).
37. U.S. Energy Information Administration. Capacity factors for utility scale generators not primarily using fossil fuels, January 2013-August 2018. (2018). at https://www.eia.gov/electricity/monthly/epm_table_grapher.php?t=epmt_6_07_b
38. Dell, J. & Klippenstein, M. Wind Power Could Blow Past Hydro's Capacity Factor by 2020. (2018). at <https://www.greentechmedia.com/articles/read/wind-power-could-blow-past-hydros-capacity-factor-by-2020>
39. Wind-turbine-models.com. General Electric GE 1.85 - 87. (2018). at https://www.en.wind-turbine-models.com/turbines/745-general-electric-ge-1.85-87
40. Global Wind Energy Council. *Global Wind Energy Outlook 2018* (2018).
41. Hughes, G. *The Performance of Wind Farms in the United Kingdom and Denmark* (the Renewable Energy Foundation, 2012).
42. Morice, C. P., Kennedy, J. J., Rayner, N. A. & Jones, P. D. Quantifying uncertainties in

global and regional temperature change using an ensemble of observational estimates: The HadCRUT4 data set. *J. Geophys. Res. Atmos.* **117,** 1–22 (2012).

43. Reynolds, R. W., Rayner, N. A., Smith, T. M., Stokes, D. C. & Wang, W. An improved in situ and satellite SST analysis for climate. *J. Clim.* **15,** 1609–1625 (2002).

Additional information

Supplementary information is available in the online version of the paper. Reprints and permissions information is available online at www.nature.com/reprints.

Correspondence and requests for materials should be addressed to Z. Zeng.

Acknowledgements

This study was supported by the Strategic Priority Research Program of Chinese Academy of Sciences (grant no. XDA20060402), the start-up fund provided by Southern University of Science and Technology (29/Y01296122) and Lamsam-Thailand Sustain Development (B0891). L. Li was partially supported by the National Key Research and Development Program of China (Grant-2018YFC1507704). J. Liu was supported by the National Natural Science Foundation of China (41625001). We thank Della Research Computing in Princeton University for providing computing resources. We thank the U.S. National Climatic Data Center and the U.K. Met Office Hadley Centre for providing surface wind speed measurements, and thank the Program for Climate Model Diagnosis and Intercomparison and the IPSL Dynamic Meteorology Laboratory for providing surface wind speed simulations.

Author contributions

Z. Zeng and E. Wood designed the research. Z. Zeng and L. Yang performed analysis; Z. Zeng, A. Ziegler, T. Searchinger wrote the draft; and all the authors contributed to the interpretation of the results and the writing of the paper.

Data availability. The data for quantifying wind speed changes are the Global Surface Summary of the Day database (GSOD, ftp://ftp.ncdc.noaa.gov/pub/data/gsod), and the HadISD (version v2.0.2.2017f) global sub-daily database (https://www.metoffice.gov.uk/hadobs/hadisd/). The time series of climate indices describing monthly atmospheric and oceanic phenomena are obtained from the National Oceanic and Atmospheric Administration (https://www.esrl.noaa.gov/psd/data/climateindices/list/). Simulated wind speed changes in Coupled Model Intercomparison Project Phase 5 (CMIP5) are available in the Program for Climate Model Diagnosis and Intercomparison (https://esgf-node.llnl.gov/projects/cmip5/). Simulated wind speed changes constrained by historical sea surface temperature are provided by the IPSL Dynamic Meteorology Laboratory. Wind records in reanalysis products include the ECMWF ERA-Interim Product (apps.ecmwf.int/datasets/data/interim-full-daily/), the ECMWF ERA5 Product (https://cds.climate.copernicus.eu/cdsapp#!/dataset/reanalysis-era5-single-levels-monthly-means) and the NCEP/NCAR Global Reanalysis Product (http://rda.ucar.edu/datasets/ds090.0/). The processed wind records and the relevant code are available in Supplementary Data 1 and 2 (https://doi.org/10.6084/m9.figshare.9917246.v2). All datasets are also available on request from Z. Zeng.

Code availability. The program used to generate all the results is MATLAB (R2014a) and ArcGIS (10.4). Analysis scripts are available at https://doi.org/10.6084/m9.figshare.9917246.v2. The code producing wind records are available in Supplementary Data 1 and 2.

Competing financial interests

The authors declare no competing financial interests.

Methods

Wind datasets. The key data used in this analysis is the Global Surface Summary of the Day (GSOD) database processed by the National Climatic Data Center (NCDC) of the U.S. (download August 1st 2018 from ftp://ftp.ncdc.noaa.gov/pub/data/gsod). The database is derived from the United States Air Force (USAF) DATSAV3 Surface data and the Federal Climate Complex Integrated Surface Hourly dataset grounding on data exchanged under the World Meteorological Organization (WMO) World Weather Watch Program according to WMO Resolution 40 (Cg-XII)[44]. There is a total of 28,149 stations included in the GSOD database globally (for the distributions see the dots in Supplementary Fig. 3). The original records from all the weather stations have undergone extensive quality control procedures (more than 400 algorithms, see www.ncdc.noaa.gov/isd for details). These synoptic hourly observations were processed into mean daily values from recorded hourly data by NCDC.

We focus our study on the decadal variation of u and other wind variables (maximum sustained wind speed, maximum wind gust) for the 40-year period of 1978-2017, when the data are the most complete. In selection of the final subset of stations, we employ strict selection criteria to avoid including incomplete data series. Firstly, we only select stations with complete data for all the 40 years of the analysis (1978-2017), each year with complete records for all the 12 months. Secondly, each monthly value has to be derived from at least 15 days of data. Finally, the daily values have to be derived from a minimum of four observations. As a result, only 1,435 stations are included for analysis (locations are shown in Supplementary Fig. 3; and the mean number of observations in a day is shown in Supplementary Fig. 10; code and the processed data is available in Supplementary Data 1). Among them, 543 stations are automatic monitoring stations that are in operation during the entire study period. For some analyses (Supplementary Fig. 7) we relax our selection criteria to include more stations – for instance, by allowing 1, 5, 10 or 20 years of missing data. Last, the results show no dependence on whether global mean annual *u* or global median annual *u* is used to describe the decadal variation of global *u* (Supplementary Fig. 21 versus Fig. 1a).

We also repeat the wind analyses using the HadISD (version v2.0.2.2017f)[24] global sub-daily database, which is distributed by the Met Office Hadley Centre and is freely accessed from: https://www.metoffice.gov.uk/hadobs/hadisd/. The total number of stations in HadISD is 8,103, all of which passed quality control tests that are designed to remove bad data while keeping the extremes of wind speed and direction, temperature, dew point temperature, sea-level pressure, and cloud data (total, low, mid and high level). For example, a set of quality control procedures[24] (e.g., duplicate check, distributional gap check, neighbor outlier check, and so on) has been performed on the major climatological variables. In our analysis, we use the criteria that is described above to select stations that have uninterrupted, continuous monthly records during the period 1978-2017 (n = 1,542; code and the processed data is available in Supplementary Data 2).

Climate indices. The dynamics of ocean/atmospheric circulations can be described with climate indices. Almost all climate indices are associated to some extent with regional surface temperature anomalies (or temperature heterogeneity), in particular sea surface temperature (SST). We select twenty-one time series of climate indices describing monthly atmospheric and oceanic phenomena to compare decadal variations of the Earth's climate system with changes in wind speed (Supplementary Table 2). Only indices that are available for the whole study period

(1978-2017) are considered (downloaded from https://www.esrl.noaa.gov/psd/data/climateindices/list/). For example, we include the following eight teleconnection indices: Pacific Decadal Oscillation (PDO); Pacific North American Index (PNA); Western Pacific Index (WP); North Atlantic Oscillation (NAO); East Pacific/North Pacific Oscillation (EP/NP); North Pacific pattern (NP); East Atlantic pattern (EA); and Scandinavia pattern (SCAND). We include one atmospheric index (Arctic Oscillation (AO)) and one multivariate El Niño–Southern Oscillation (ENSO) index. We include six indices describing regional SST in Pacific oceans: Eastern Tropical Pacific SST (5^{o}N – 5^{o}S, 150^o W – 90 ^{o}W) (NINO3); Central Tropical Pacific SST (5^{o}N-5^{o}S) (160^{o}E-150^{o}W) (NINO4); Extreme Eastern Tropical Pacific SST (0 – 10^{o}S, 90^{o}W – 80^{o}W) (NINO12); East Central Tropical Pacific SST (5^{o}N – 5^{o}S) (170^{o}W – 120^{o}W) (NINO34); Oceanic Nino Index (ONI); and Western Hemisphere warm pool (WHWP). Two of the indices describe regional SST in Atlantic oceans—the Tropical Northern Atlantic Index (TNA) and the Tropical Southern Atlantic Index (TSA). The final three indices are the Atlantic Meridional Mode (AMM), the Southern Oscillation Index (SOI), and the 10.7-cm Solar Flux (Solar). All these indices are widely used by the climate community and are informative regarding the decadal variations of ocean/atmospheric circulations.

Statistical analyses. It is apparent that the trend varies in the time series of global and/or regional average mean annual u for different ranges of year (e.g., Fig. 1a). A traditional single linear model does not provide an adequate description of a change in the tendency. Therefore, we apply a piecewise linear regression model[22,23] to quantify potential turning points in a given time series. Piecewise linear regression is capable of detecting where the slope of a linear function changes, and allows multiple linear models to be fitted to each distinct section of the time series.

For a time series y (e.g. global average mean annual *u*), a continuous piecewise linear regression model with one turning point (TP) can be described as:

$$y = \begin{cases} \beta_0 + \beta_1 t + \varepsilon, & t \le TP \\ \beta_0 + \beta_1 t + \beta_2 (t - TP) + \varepsilon, & t > TP \end{cases} \tag{3}$$

where t is year; β_0 , β_1 and β_2 are regression coefficients; and ε is the residual of the regression. The linear trend is β_1 before the TP (year), and $\beta_1 + \beta_2$ after the TP. We use least square error techniques to fit the model to the data and determine TP, β_0 , β_1 and β_2 . To avoid linear regression in a period with too few years, we confine TP to be within the period of 1980 to 2015. The necessity of introducing TP is tested statistically with the *t*-test under the null hypothesis that "β_2 is not different from zero". The diagnostic statistics for the regression also include the goodness of fit (R^2), the P value for the whole model, and the P values for the trends before and after TP. We consider $P < 0.05$ as significant.

In addition, we use a forward stepwise regression algorithm[27] to select major climate indices that have the largest explanatory power for the decadal variations in *u*. The algorithm is a systematic method for adding predictors from a multilinear model according to their statistical significance in explaining the response (decadal variation of *u* in this study). The initial regression model contains only an intercept term. The explanatory power of incrementally larger and smaller models is then compared to determine which predictor should be included. At each step, the P-value of an F-statistic is calculated to examine models with a potential predictor that is not already in the model. The null hypothesis is that the predictor has a zero coefficient if included in the model. If there is sufficient evidence at a given significant level to reject the null hypothesis, the predictor is added to the model. Therefore, the earlier the predictor enters in to the model, the larger the explanatory power the predictor has.

We apply the forward stepwise regression to determine six climate indices (referred as major indices hereafter) from a generalized linear model according to their statistical significance in explaining *u*. We use only six indices in the regression because the fit improvement becomes marginal when the number of indices retained in the stepwise regression is greater. The regression model is then applied to reconstruct interannual variations of *u* over the globe and/or the regions using the selected six climate indices. The forward stepwise regression is first applied to the original time series considering the total variances, and then applied to the detrended time series to exclude the variances from linear trends (Supplementary Figs 15 and 16). Last, to test whether these climate indices can be used to predict *u*, we further train the models using only the detrended time series before the turning points; we then compare the reconstructed *u* with the observed *u* after the turning points (Fig. 2).

Analyses on the possible causes for the interannual variability of wind speed. Globally, the indicators (climate indices) significantly correlated with *u* include TNA ($R = -0.50$; P-value < 0.01), PDO ($R = 0.46$; $P < 0.01$), WHWP ($R = -0.46$; $P < 0.01$), NAO ($R = 0.39$; $P < 0.05$), AMM ($R = -0.39$; $P < 0.05$), EP/NP ($R = 0.37$; $P < 0.05$), TSA ($R = -0.38$; $P < 0.05$), Solar ($R = 0.35$; $P < 0.05$), SOI ($R = -0.32$; $P < 0.05$), and EA ($R = 0.31$; $P < 0.05$). Overall, the twenty-one climate indices explain 90% of the interannual variation in global mean annual *u* (adjusted $R^2 =$ 78%). Regionally, they explain 91%, 75% and 87% of the interannual variation in mean annual *u* for North America (adjusted R^2 = 81%), Europe (adjusted R^2 = 46%) and Asia (adjusted R^2 = 71%), respectively.

To avoid overfitting, we use stepwise linear regression to discuss whether multiple regression of six indices can reconstruct interannual variations of *u* over the globe and/or regions. To estimate the uncertainty associated with samples, we randomly select 40% of stations for the calculation of global/regional *u* and repeat the analyses 300 times. The number in parentheses in Supplementary Table 3 shows how many times climate indices are selected as six major predictors. These climate indices explain 70 ±5%, 79 ±3%, 48 ±9%, and 51 ±8% of the interannual variation in mean annual *u* for the globe, North America, Europe, and Asia, respectively (Supplementary Table 3, Supplementary Fig. 15). Furthermore, we also test stepwise regression analysis after detrending all data, although this adjustment may mask relationships underlying long term stilling. The goodness of fit decreased as expected when the stilling trend is removed (Supplementary Fig. 16). Yet, detrended indices still significantly explain detrended variation of *u*, in particular the recent reversal (Supplementary Fig. 16), supporting the robustness of the regression analyses.

The greatest explanatory power factor for each region is associated with the following indices: TNA for North America ($R = -0.67$, $P < 0.001$); NAO for Europe ($R = 0.37$, $P < 0.05$); and PDO for Asia ($R = 0.50$, $P < 0.01$) (Supplementary Tables 2 and 3). These three indices are also significantly correlated with global mean annual *u* ($P < 0.01$; Supplementary Table 2). We further conduct Granger causality tests[45], in which we select lag length using a Bayesian information criterion. Global mean annual *u* is "Granger caused" by TNA ($P < 0.001$), NAO (P <

0.01) and PDO ($P < 0.1$). Regionally, the tests also reject the null hypothesis that (a) TNA does not Granger cause *u* over North America ($P < 0.001$), (b) NAO does not Granger cause *u* over Europe ($P < 0.1$), and (c) PDO does not Granger cause *u* over Asia ($P = 0.11$). In addition, although the reversal of winds and the retained climate indices differ in regions, owing to ocean/atmosphere oscillations having some degree of synchronization during turning points of multidecadal climate variability[46], the pattern of terrestrial stilling and its reversal seems to be synchronized.

PDO and TNA are important predictors regardless of the subset of stations used. Yet, while NAO has the largest explanatory power for regional *u* over Europe, there are 169/300 cases that NAO is not included as a major predictor (Supplementary Table 3). Thus, even within Europe, the impact of NAO differs regionally. We thus investigate the spatial patterns of the correlation between the three indices (PDO, TNA, NAO) and the regional winds (Fig. 3c-e). The regional wind is calculated using all stations within a $5^{o} \times 5^{o}$ cell; and only the cells with more than three stations are included in the analysis. TNA has a strong, significant negative correlation with regional *u* in North America excluding western Canada and areas near Mexico (Fig. 3c). PDO has a significant positive correlation with regional *u* globally (Fig. 3e). NAO has overwhelmingly significant positive correlation with regional *u* in the U.S. and Northern Europe, in particular the U.K.. In contrast it has a negative correlation with regional *u* in Southern Europe (Fig. 3d). Statistically, NAO is negatively correlated with European winds south of 48^{o}N ($R = -0.39$, $P < 0.05$); in contrast, it is significantly and positively correlated with European winds north to 48^{o}N ($R = 0.48$, $P < 0.01$).

Calculations for wind power assessments. Due to the nonlinear relationship between wind power (p) and wind speed (u) (Equation (1)), high temporal resolution data are needed for u to produce an accurate estimate of p. Thus, we use the HadISD global sub-daily database from the Met Office Hadley Centre[24]. For each station that has uninterrupted, continuous monthly records during the period 1978-2017 (n = 1,542), we use linear interpolation to interpolate a sub-daily time series to an hourly time series. Fig. 4a shows the frequency distributions of global average hourly wind speed in 2010 and 2017, and the year 2024, assuming the same increasing rate.

We then discuss annual wind power production given these hourly wind speed time series for 2010, 2017 and 2024, considering that production is dependent on the specifications of wind turbines. Here we use General Electric GE 2.5 – 120 (ref. 34) as an example. The parameters for this turbine include the following: rated power, 2,500.0 kW; cut-in wind speed, 3.0 m s^{-1}; cut-out wind speed, 25.0 m s^{-1}; diameter, 120 m; swept area, 11,309.7 m^2; and hub height: 110/139 m (here we take 120 m). The power curve for this turbine is shown in Supplementary Fig. 22. The wind speed time series (2010, 2017 and 2024) at the height of the turbine (i.e. 120 m) are first estimated using the wind profile power law (Equation (2)), and are then converted into the hourly wind power (Supplementary Fig. 19) using the power curve (Supplementary Fig. 22). Owing to the increased frequency of high u, annual wind power production from the turbine increases from 2.4 million kWh in 2010 to 2.8 million kWh in 2017, and then to 3.3 million kWh in 2024. As a result, the overall capacity factor increases 1.9% during 2010-2017, and 2.2% during 2018-2024.

To compare the significance of the increased capacity factor induced by the strengthening u with that due to technology innovation (e.g. improvement of the turbine's power efficiency), we collect the overall capacity factor for wind generation in the U.S. from the U.S. Energy Information Administration[37] (the black line in Fig. 4b). In the U.S., the overall capacity factor is highly correlated with the cube of regional wind speed (u^3) (R = 0.86, P < 0.01; Fig. 4b). Even for the detrended time series, the correlation coefficient between capacity factor and u^3 is as high as 0.71 (P < 0.05), showing that wind speed is a key factor for the year-to-year variation of wind power energy production. It is well known that technology innovation is a key factor that drives the increase of capacity factor for wind generation[38]. To isolate the *u*-induced increase in capacity factor from that due to technology innovation, we use the regional mean hourly wind speed in 2010, 2017 and 2024 (assuming the same increasing rate) to estimate the increase of capacity factor for a given turbine, thereby controlling for technology innovation. The *u*-induced increase in capacity factor is +2.5% between 2010 and 2017, and +3.2% between 2017 and 2024. It explains more than 50% of the overall increase of capacity factor for wind generation in the U.S..

We also collect information regarding the installed turbines from the U.S. Wind Turbine Database (n = 57,646; https://eerscmap.usgs.gov/uswtdb) (locations refer to Supplementary Fig. 23). The turbine with the nearest distance to one of the HadISD weather stations (n = 1,542) is at Deaf Smith County, the U.S. (<1 km; wind farm name: Hereford 1; case ID: 3047384; location see the inset plot in Fig. 4c). The turbine was installed in 2014. The turbine is a General Electric GE 1.85 – 87 (ref. 39). The parameters for this turbine include: rated power, 1,850.0 kW; cut-in wind speed, 3.0 m s^{-1}; rated wind speed, 12.5 m s^{-1}; cut-out wind speed, 25.0 m s^{-1}; diameter, 87.0 m; swept area, 5,945.0 m^2; hub height: 80 m. We combine these parameters with Equation (1) to estimate the power curve for the turbine (Supplementary Fig. 24). Finally, we integrate the power curve with the hourly wind speed from 1978 to 2017 at the hub height at this station to calculate annual wind power production generated by the General Electric GE 1.85 – 87 turbine (Supplementary Fig. 25a; red bars in Fig. 4d). In addition, we calculate annual wind power production at the station generated by the General Electric GE 2.5 – 120 turbine (Supplementary Fig. 25b; green bars in Fig. 4d). We also use the Equation (1) to estimate maximum annual wind power production at the station given diameter of 120 m and hub height of 120 m (the same as the General Electric GE 2.5 – 120 turbine), which is constrained by the Betz Limit (f = 16/27 in Equation (1)) (Supplementary Fig. 25c; blue bars in Fig. 4d). The Beltz Limit describes the theoretical maximum ratio of power that can be extracted by a wind turbine to the total power contained in the wind.

References.

44. WMO Resolution 40 (Cg-XII). *Exchanging meteorological data: Guidelines on relationships in commercial meteorological Aativities: WMO policy and practice* (WMO, 1996).

45. Granger, C. W. J. Investigating causal relations by econometric models and cross-spectral methods. *Econometrica* **37,** 424–438 (1969).

46. Henriksson, S. V. Interannual oscillations and sudden shifts in observed and modeled climate. *Atmos. Sci. Lett.* **19,** e850 (2018).

47. National Centers for Environmental Prediction/National Weather Service/NOAA/U.S. Department of Commerce, NCEP/NCAR Global Reanalysis Products, 1948-continuing, http://rda.ucar.edu/datasets/ds090.0/, Research Data Archive at the National Center for Atmospheric Research, Computational and Information Systems Laboratory, Boulder, Colo. (Updated monthly.) Accessed 10 AUG 2018.

48. European Centre for Medium-Range Weather Forecasts, ERA-Interim Project,

https://doi.org/10.5065/D6CR5RD9, Research Data Archive at the National Center for Atmospheric Research, Computational and Information Systems Laboratory, Boulder, Colo. (Updated monthly.) Accessed 10 AUG 2018.

49. Copernicus Climate Change Service (C3S) (2017): ERA5: Fifth generation of ECMWF atmospheric reanalyses of the global climate. https://cds.climate.copernicus.eu/cdsapp#!/home, Copernicus Climate Change Service Climate Data Store (CDS), Assessed 25 May 2019.

50. Zhu, Z. *et al.* Global data sets of vegetation leaf area index (LAI)3g and fraction of photosynthetically active radiation (FPAR)3g derived from global inventory modeling and mapping studies (GIMMS) normalized difference vegetation index (NDVI3G) for the period 1981 to 2011. *Remote Sens.* **5,** 927–948 (2013).

51. Liu, X. *et al.* High-resolution multi-temporal mapping of global urban land using Landsat images based on the Google Earth Engine Platform. *Remote Sens. Environ.* **209,** 227–239 (2018).

Figure Legends.

Figure 1. Turning point for mean global surface wind speed (*u*). (**a**) Global mean annual *u* during 1978-2017 (black dot and line). The piecewise linear regression model indicates a statistically significant turning point in 2010. The red line is the piecewise linear fit (R^2 = 90%, $P < 0.001$). The dashed line indicates the turning point. The trends before and after the turning point are shown in the inset. Each grey line (n = 300) is a piecewise linear fit for a randomly selected subset (40%) of the global stations. (**b**) Frequency distribution of the estimated turning points derived from 300 resampling results. (**c**) Frequency distribution of the trends in mean annual *u* before and after the turning points identified inthe 300 resampling results. The result is based on the weather stations in the GSOD database.

Figure 2. Factors driving the decadal variations in *u*. Observed (black) and reconstructed (red) detrended mean annual *u* over the following: (a) the globe, (b) North America, (c) Europe, and (d) Asia. The models are trained using only the detrended time series before the turning points. The dashed line indicates the turning point (2010 for the globe, 2012 for North America, 2003 for Europe, and 2001 for Asia). For the globe and each of the three continents, we select six largest explanatory climate indices for the decadal variations of *u* with a stepwise forwarding regression model. The selected climate indices are then used to reconstruct decadal variations of *u* via a multiple regression. Uncertainties are the inter-quartile range of the results based on a randomly selected 40% subset of the station pools (repeated 300 times). Inset plots indicate the locations of the stations. Inset black numbers are coefficients of determination between observed and reconstructed *u* before the turning points. Inset red numbers are correlation coefficient and its significance between observed and reconstructed *u* after the turning points.

Figure 3. Mechanisms for the decadal variation in *u*. Normalized mean annual surface temperature for the years with negative (**a**) and positive (**b**) anomalies of detrended wind. Characteristic regions for Pacific Decadal Oscillation (PDO), North Atlantic Oscillation (NAO) and Tropical Northern Atlantic Index (TNA) are outlined by green, red, and blue polygons, respectively. Surface temperature over land is obtained from Climate Research Unit TEM4 with a spatial resolution of 5° by 5° (ref. 42), and that over ocean is from NOAA Optimum Interpolation (OI) Sea Surface Temperature V2, with a spatial resolution of 1° by 1° (ref. 43). Spatial patterns of the correlation between the regional ($5^{o} \times 5^{o}$) mean annual u and the following: (**c**) TNA; (**d**) NAO; and (**e**) PDO for 1978-2017. Dotting represents significant at $P < 0.05$ level. Decadal variations are shown in panels (**f**) for TNA and regional u in North America; (**g**) for NAO and regional u in Europe; and (**h**) for PDO and regional u in Asia. The thin lines are annual values; and the thick lines are 9-year-window moving averages. The black lines are wind speed; and each of the colored lines are TNA, NAO, and PDO, respectively.

Figure 4. Implications of the recent reversal in global terrestrial stilling for wind energy industry. (**a**) Frequency distribution of global mean hourly u in 2010 and 2017, and the year 2024 assuming the same increasing rate. (**b**) Time series of the overall capacity factor for wind generation in the U.S. (black line) and the cube of the regional-average u (u^3; blue line) from 2008 to 2017. The inset scatter plot shows the significant relationship between the overall capacity factor and the regional u^3 ($R = 0.86$, $P < 0.01$). The inset black numbers show the trend in the overall capacity factor for wind generation, and the inset red numbers show the u-induced increase of capacity factor in the U.S.. (**c**) Mean annual u observed at a weather station near an installed turbine at Deaf Smith County in the U.S. (<1 km;location shown in the inset). The turbine was installed in 2014. The background colors separate different periods: P0, the 1980s

level when u is relative strong (1978-1995); P1, the evaluation years before the installation of the turbine (2009-2013); P2, the operation years when the turbine was generating power (2014-2017). (**d**) Mean annual wind power production at Deaf Smith County from different wind turbines during the three periods of reference (grey: General Electric GE 1.85 – 87; green: General Electric GE 2.5 – 120 turbine; blue: the theoretical maximum ratio of power that can be extracted by a wind turbine given diameter of 120 m and hub height of 120 m). Error bars show the interannual variability within the periods.

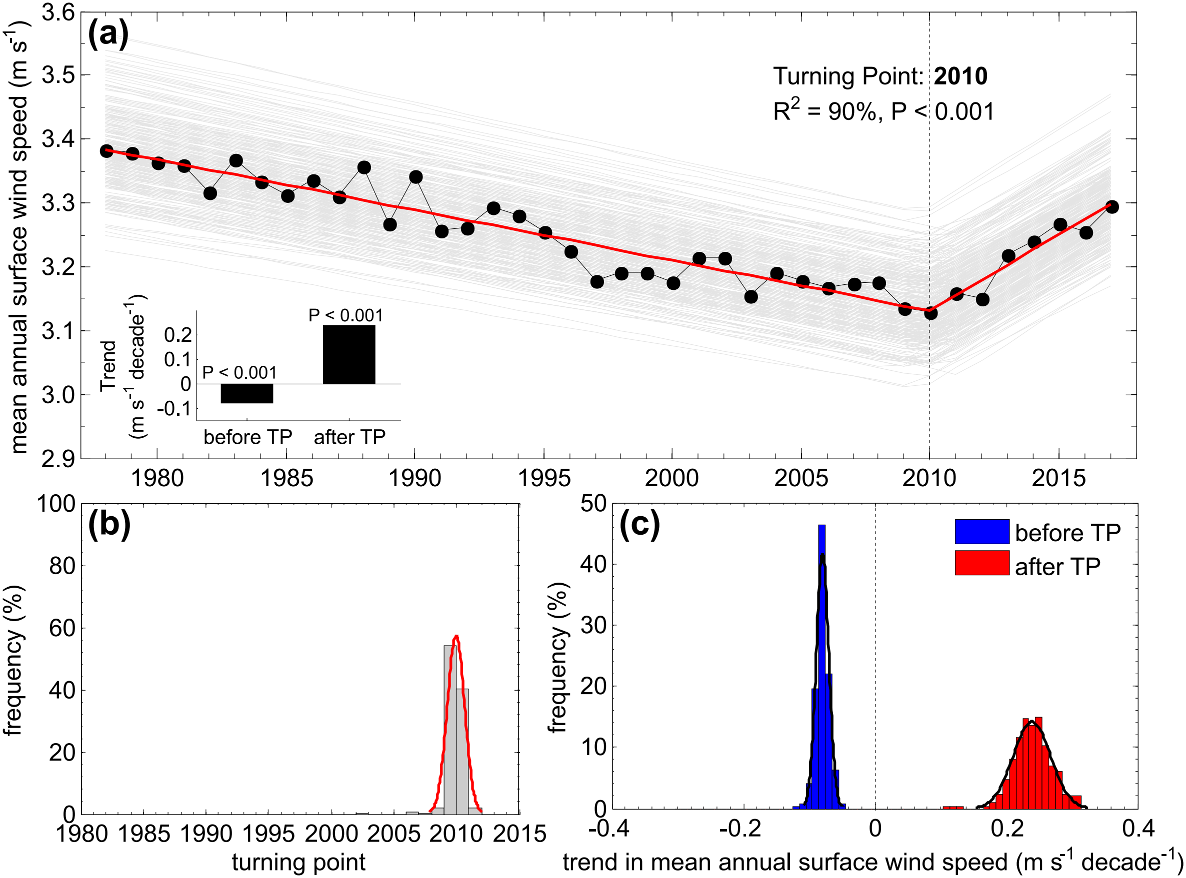

(a)
Turning Point: **2010**
R^2 = 90%, P < 0.001
mean annual surface wind speed (m s^{-1})
Trend (m s^{-1} decade^{-1})
P < 0.001
P < 0.001
before TP
after TP
(b)
frequency (%)
turning point
(c)
before TP
after TP
frequency (%)
trend in mean annual surface wind speed (m s^{-1} decade^{-1})

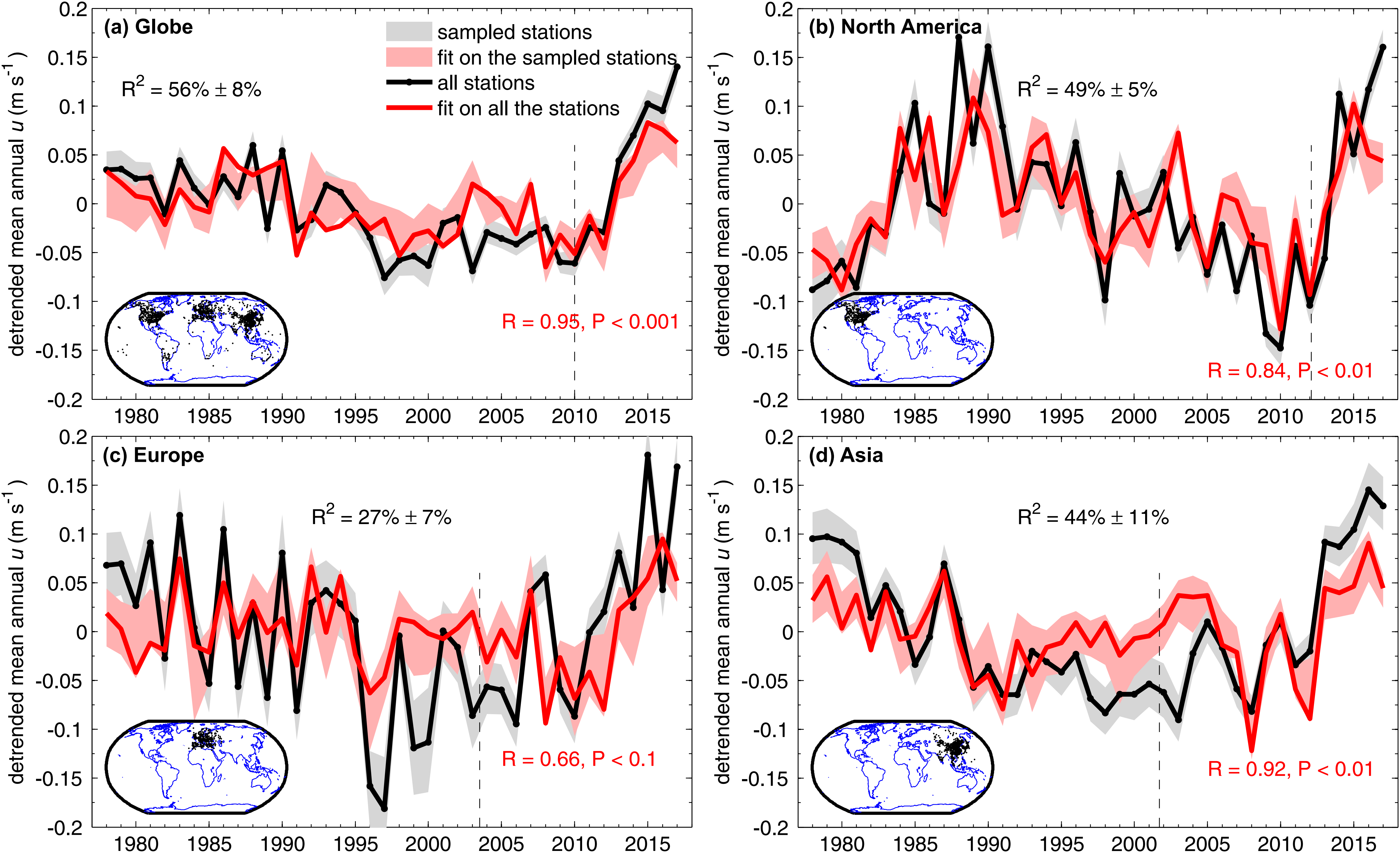

(a) Globe
sampled stations
fit on the sampled stations
all stations
fit on all the stations
R2 = 56% ± 8%
R = 0.95, P < 0.001
(b) North America
R2 = 49% ± 5%
R = 0.84, P < 0.01
(c) Europe
R2 = 27% ± 7%
R = 0.66, P < 0.1
(d) Asia
R2 = 44% ± 11%
R = 0.92, P < 0.01
detrended mean annual u (m s-1)
0.2
0.15
0.1
0.05
0
-0.05
-0.1
-0.15
-0.2
1980
1985
1990
1995
2000
2005
2010
2015

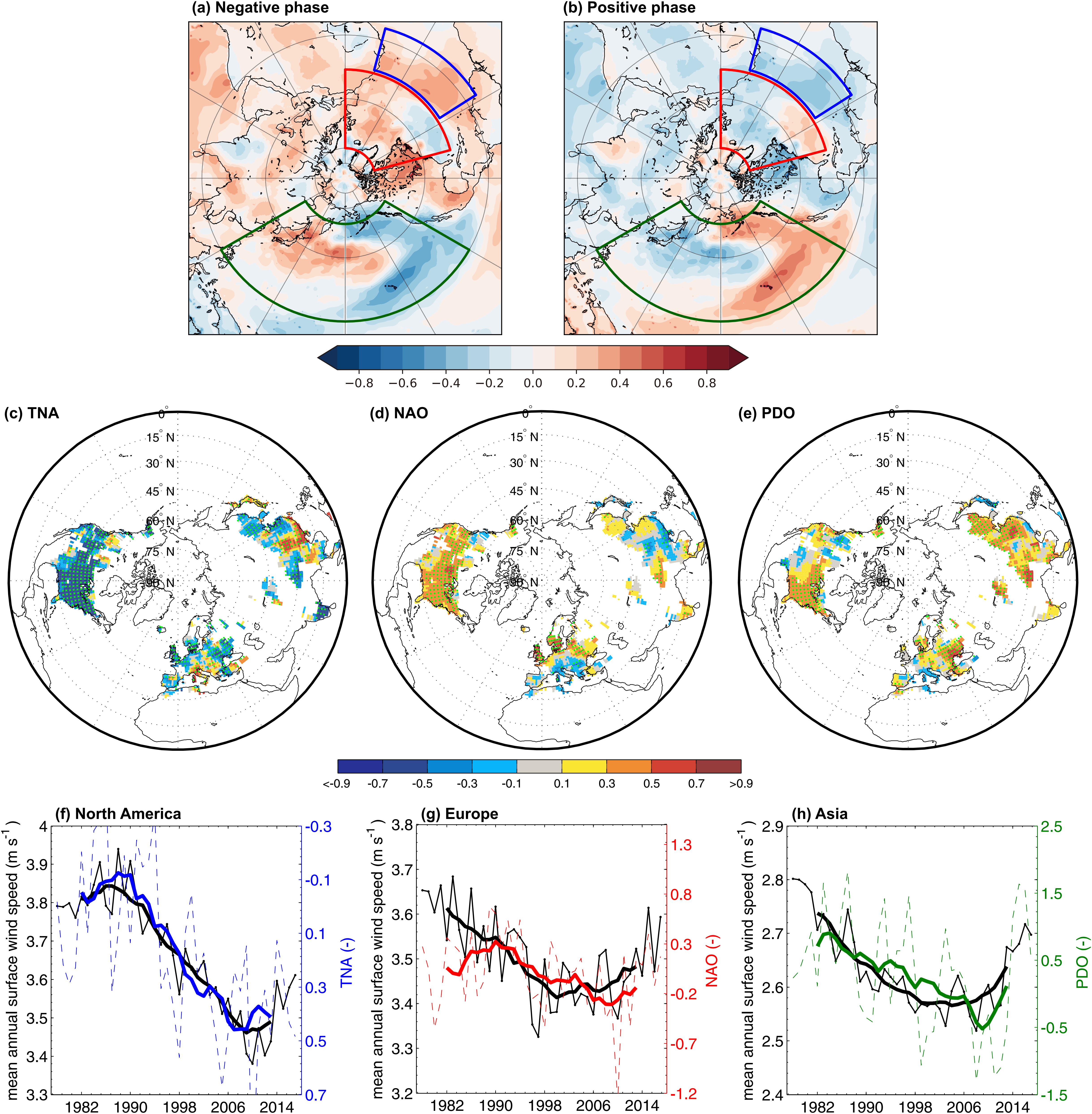

(a) Negative phase
(b) Positive phase
−0.8 −0.6 −0.4 −0.2 0.0 0.2 0.4 0.6 0.8
(c) TNA
(d) NAO
(e) PDO
0°
15° N
30° N
45° N
60° N
75° N
90° N
<-0.9 -0.7 -0.5 -0.3 -0.1 0.1 0.3 0.5 0.7 >0.9
(f) North America
(g) Europe
(h) Asia
mean annual surface wind speed (m s^{-1})
TNA (-)
NAO (-)
PDO (-)
1982 1990 1998 2006 2014

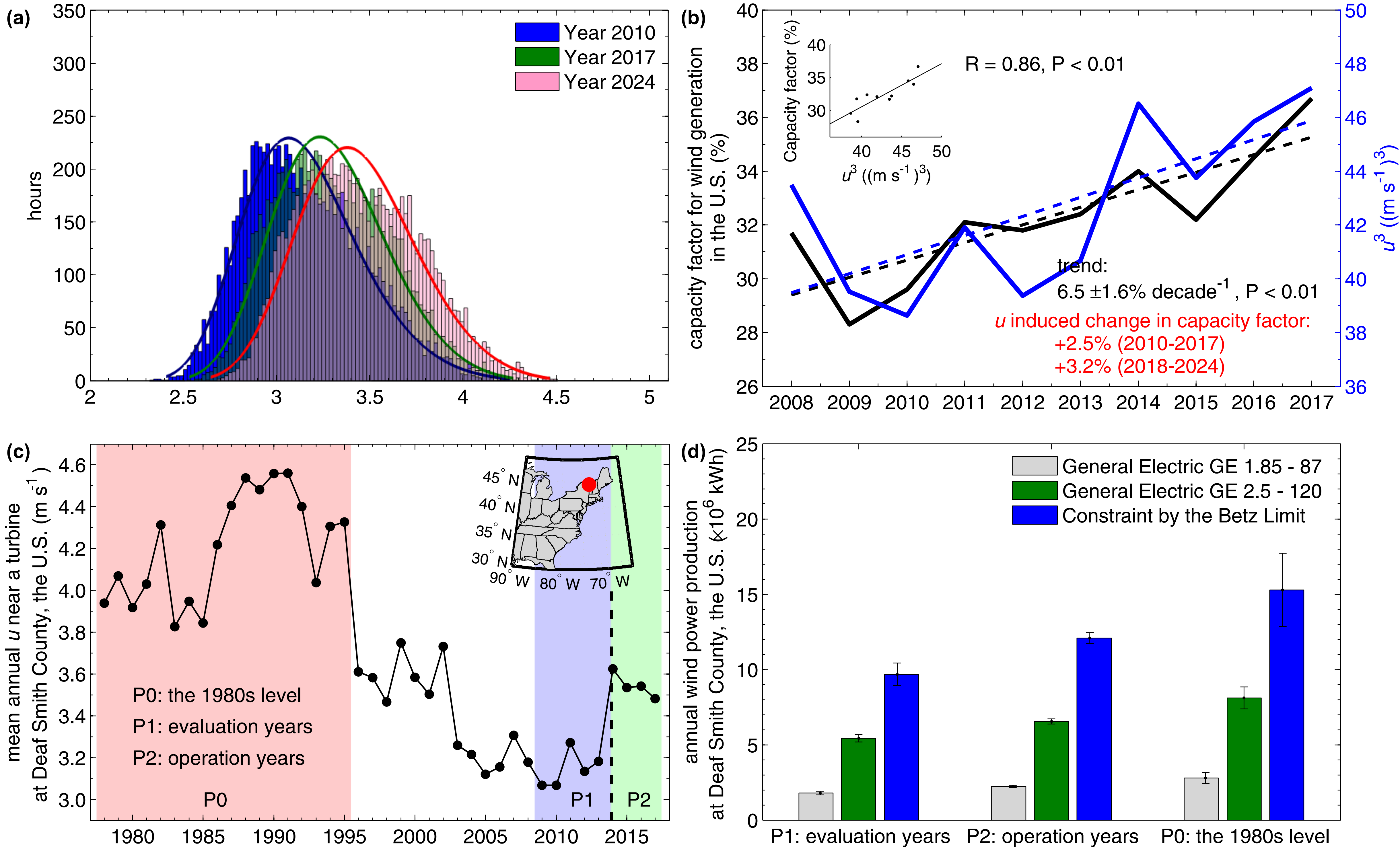

(a)
Year 2010
Year 2017
Year 2024
hours
(b)
capacity factor for wind generation in the U.S. (%)
Capacity factor (%)
u³ ((m s⁻¹)³)
R = 0.86, P < 0.01
trend:
6.5 ±1.6% decade⁻¹, P < 0.01
u induced change in capacity factor:
+2.5% (2010-2017)
+3.2% (2018-2024)
(c)
mean annual u near a turbine at Deaf Smith County, the U.S. (m s⁻¹)
45° N
40° N
35° N
30° N
90° W
80° W
70° W
P0: the 1980s level
P1: evaluation years
P2: operation years
P0
P1
P2
(d)
annual wind power production at Deaf Smith County, the U.S. (×10⁶ kWh)
General Electric GE 1.85 - 87
General Electric GE 2.5 - 120
Constraint by the Betz Limit
P1: evaluation years
P2: operation years
P0: the 1980s level